

Article

Microstructural Transformation and High-Temperature Aluminum Corrosion Properties of Co-Based Alloy Coating Prepared by Laser Cladding

Rui Liu [†], Mengyu Zhang ^{*,†}, Jiacheng Yu, Qifan Yang and Shiyu Gao ^{*}

Key Laboratory of Advanced Forging and Stamping Technology and Science, Ministry of Education, Yanshan University, Qinhuangdao 066004, China; zrrleo@stumail.yzu.edu.cn (R.L.); yujiachengnew@sina.com (J.Y.); y1056461200@sina.com (Q.Y.)

* Correspondence: zhangmengyunew@sina.com (M.Z.); gao58@sina.com (S.G.)

† These authors contributed equally to this work.

Abstract: A Co-based alloy coating was deposited on H13 steel substrate via pulsed Nd:YAG laser and the corrosion resistance to and mechanism of corrosion in molten aluminum were explored. The results showed that the coating was mainly composed of γ -Co dendrite and $M_{23}C_6$ precipitation. The average hardness in the cladding layer was 732.6 HV_{0.5}, which was 3.55 times greater than that of the H13 substrate. During the molten aluminum corrosion test, the surface of the Co-based alloy coating was immersed for 4, 8, 16 and 24 h at 700 °C. The corrosion rate decreased with increases in aluminum erosion time. It was observed that there were two intermediate layers between the coating and the liquid Al, with (Co, Fe, Cr)₂Al₉ intermetallic compounds (IMCs) layer near the coating side and the (Fe, Cr)₄Al₁₃ and (Co, Fe, Cr)₂Al₅ intermetallic compounds (IMCs) layer near the Al solidification side. After 24 h of static corrosion, the Co-based alloy coating could still maintain its integrity to protect the substrate.

Keywords: laser cladding; Co-based alloy; microstructure evolution; molten aluminum corrosion



Citation: Liu, R.; Zhang, M.; Yu, J.; Yang, Q.; Gao, S. Microstructural Transformation and High-Temperature Aluminum Corrosion Properties of Co-Based Alloy Coating Prepared by Laser Cladding. *Coatings* **2022**, *12*, 603. <https://doi.org/10.3390/coatings12050603>

Academic Editor: Claudia Barile

Received: 12 April 2022

Accepted: 26 April 2022

Published: 28 April 2022

Publisher's Note: MDPI stays neutral with regard to jurisdictional claims in published maps and institutional affiliations.



Copyright: © 2022 by the authors. Licensee MDPI, Basel, Switzerland. This article is an open access article distributed under the terms and conditions of the Creative Commons Attribution (CC BY) license (<https://creativecommons.org/licenses/by/4.0/>).

1. Introduction

The traditional manufacturing processes for aluminum alloys include hot extrusion forming, forge forming, deep drawing forming, casting forming, hot-dip aluminizing, and others [1–4]. Liquid aluminum, which exhibits high chemical activity and corrosiveness, can react with nearly all other metals and metal oxides due to its affinity [5]. Therefore, system failure caused by corrosion from molten aluminum is inevitable for crucibles, die-casting molds and sleeves [6,7]. In order to deal with these problems, surface treatment technology, a cost-effective method to protect the surface of the material, has been widely used in the study of resistance to liquid aluminum corrosion.

One of the surface treatment methods, the laser cladding process, is a new remanufacturing technology. With the rapid development in the laser field, the laser cladding process is now widely applied in surface modification, repair and remanufacturing of products [8–11]. In previous studies, various surface strengthening processes were used to improve the resistance of materials to molten aluminum corrosion. These include boronizing, nitriding, chemical vapor deposition, physical vapor deposition, electroless plating, thermal spraying, etc. However, there are few studies on the application of laser cladding to enhance the resistance of materials to liquid aluminum corrosion. Joshi et al. [12] explored the thermal corrosion behavior of H13 steel treated with surface ion nitriding when immersed in liquid aluminum, which reasonably explained the formation and dissolution process of the compound layer. Khan et al. [13] fabricated MoB- and Co-based cermet coatings on a die steel substrate via surface dynamic spraying and tested the properties of the coating and its resistance to liquid aluminum corrosion. After a 25 h immersion test, with a

variety of borides in the coating, there were no intermetallic compounds shown between the ceramic coating and aluminum. Chen et al. [14] reported that the nitrocarburized layer on the surface of H13 steel reduced the number and thickness of intermetallic compound layers by delaying their growth kinetics, which could slow down the molten aluminum corrosion rate. López et al. [15] thermally sprayed a WC-17Co cermet coating on a carbon steel substrate. The results showed that the coating remained intact after immersion in molten aluminum for 24 h, and seemed to be an effective physical barrier to prevent the penetration of molten aluminum. These referenced studies achieved many good results, but there are still many problems regarding practical engineering applications. For example, the bonding strength between the coating and substrate is poor, the preparation of the coating is uneven, the durability of the coating in aluminum liquid is poor, the strengthening layer is thin, the cost is high, etc. Therefore, it is necessary for further study to be conducted on improving the corrosion resistance of die block steel to liquid aluminum.

As shown in previous research, a Co-based alloy laser cladding layer obtains good microstructural compositions and high-temperature mechanical properties [16,17]. At present, the research on Co-based alloy cladding layers mainly focuses on microstructure, hardness and wear resistance. Few scholars have studied the high-temperature behavior of the Co-based cladding layer, especially its corrosion resistance to molten metal. Zhao et al. [18] compared the microstructural and mechanical properties of Co-based alloy coatings prepared via laser cladding and plasma arc welding. It was found that the performance of the cladding layer was better than that of plasma arc welding coating, and mainly composed of an amorphous phase and a solid solution, with strong high-temperature wear resistance. Yan et al. [19] fabricated Co-based alloy coatings with stronger microstructural compositions and properties on a copper substrate, which overcame the difficulty of defect-free laser cladding coating on copper surfaces and greatly improved the hardness and wear resistance of the substrate. Shu et al. [20] reported a high content of the amorphous phase in the CoCrNiSiBFe high-entropy alloy cladding layer prepared on a low-carbon steel substrate, which exhibited excellent high-temperature wear resistance. Therefore, considering the good performance of Co-based alloy cladding layers, it is valuable to further investigate their corrosion resistance to molten aluminum liquid.

In this study, a Co-based alloy coating was fabricated onto a H13 steel substrate using a Nd:YAG laser. The microstructural evolution, phase composition and hardness distribution of the laser-cladding coating were investigated. The corrosion resistance of coatings to liquid aluminum was systematically studied, and the reaction mechanism was investigated in order to provide a reference for further study on corrosion resistance to liquid aluminum.

2. Materials and Experiments

2.1. Materials and Laser Cladding Procedure

In this study, H13 steel was used as substrate with dimensions of 150 mm × 100 mm × 20 mm; its chemical composition was 0.4C, 0.9Si, 0.2Mn, 4.8Cr, 1.2Mo, 1.1V with the balance being Fe (wt%). Commercial Stellite-6 Co-based self-flow alloy powder (Höganäs, Wallenberg, The Netherlands) with particle size of 45–106 µm was used as cladding material; its chemical composition is shown in Table 1. After being mechanically ground with 400 # SiC paper, the surface of the H13 steel substrate was wiped with acetone before the laser cladding process to remove oil pollution. The powder was firstly dried in a vacuum oven at 120 °C for 24 h, then pre-positioned on the substrate with a thickness of approximately 1 mm before the laser cladding process. The laser cladding process was performed using a 3000 W continuous semiconductor laser in an argon atmosphere. In this study, the following laser cladding process parameters were used: laser power was 1700 W, scanning velocity was 300 mm/min, laser beam diameter was 3 mm, overlapping rate was 50% and defocus distance was +5 mm. A macroscopic image of the laser cladding Stellite-6 Co-based alloy coating is shown in Figure 1. It is observed that the surface of the coating was generally dense and without obvious defects such as thermal cracks or pores.



Figure 1. Macroscopic morphology of the Co-based alloy coating fabricated via the laser cladding process.

Table 1. Chemical composition of the Co-based alloy powder (wt.%).

Cr	W	Fe	Ni	Mn	C	Si	Mo	Co
1.2	4.5	3.0	3.0	1.0	1.2	1.2	1.0	Bal.

2.2. Experiments

The specimens were cut into 5 mm × 5 mm × 5 mm segments using a wire electrical discharge machine in order to analyze the structural characteristics and phase constitution for a cross-section of the coating. The surface of the inlaid samples was firstly ground and polished, and then etched with a diluted nitrohydrochloric acid solution (HCL:HNO₃:H₂O = 2:1:1). The macrostructure of the coating was observed under a metallographic microscope (OM, Zeiss AX10, Oberkochen, Switzerland) and its microstructural transformation was characterized with a JSM-5610LV scanning electron microscope (SEM, JOEL, Tokyo, Japan) equipped with X-ray energy dispersive microanalysis (EDX). The phase composition of the coating was identified via Bruker-AXS D8 Advance X-Ray Diffraction (XRD, Bruker, Leipzig, Germany) with a range of 10°–90° and a scanning speed of 4°/min. Hardness tests spanning the coating were carried out on a Vickers hardness tester (Qness 200, Salzburg, Austria), in which the load was 500 g and the retention time was 10 s with a spacing distance of 0.1 mm from the surface to the substrate, as specified in ASTM E92-2017.

As for the molten aluminum erosion tests, the aluminum used was the A356 alloy, whose chemical composition is shown in Table 2. In the preparation stage, four specimens with sizes of 10 mm × 10 mm × 10 mm were cut from the cladding specimen using a wire electro-discharge machine and cleaned via ultrasonic oscillation for 360 s. The solid A356 aluminum alloy was placed in a crucible and melted in a heating furnace at 700 °C. Subsequently, the samples were immersed in the molten aluminum for 4, 8, 16 and 24 h at 700 °C. After corrosion tests, the samples were embedded, ground and polished to study their microstructural alterations and corrosion mechanisms.

Table 2. Chemical composition of the A356 aluminum alloy (wt.%).

Si	Fe	Cu	Mn	Mg	Zn	Ti	Al
6.95	0.2	0.2	0.1	0.31	0.1	0.2	Bal.

3. Results and Discussion

3.1. Microstructural Characterization

The typical cross-sectional microstructure of the St6 Co-based alloy overlapping cladding is shown in Figure 2. It is observed that the coating was free of defects such as thermal cracks and porosities, suggesting good metallurgical bonding between the cladding layer and the substrate. Measured with the Image J software, the thickness of

the coating was approximately 1 mm. There was also variation in the structural composition of the coating, as seen in the SEM images of different regions. At the bottom of the coating, the structures were mainly composed of cellular and planar grains. Away from the bonding line, they tended to transform into reticulated dendritic and columnar dendritic grains. Equiaxed and fine dendritic grains were visible at the top of the coating. From the bonding zone to the top of the cladding layer, it can obviously be characterized as the typical epitaxial growth for a solidified structure in which dendritic grains grew perpendicularly to the interface in the heat flow cooling direction. As the XRD spectra show in Figure 3, the laser cladding coating was mainly composed of the γ -Co phase (FCC) and $M_{23}C_6$ precipitation. The intensity of the γ -Co phase (FCC) peaks was much stronger than that of the $M_{23}C_6$ precipitation. According to Zhao et al. [18], γ -Co is a metastable phase, as there is insufficient incubation time to complete the $\gamma \rightarrow \epsilon$ phase transformation due to the rapid cooling rate in the laser fabrication process.

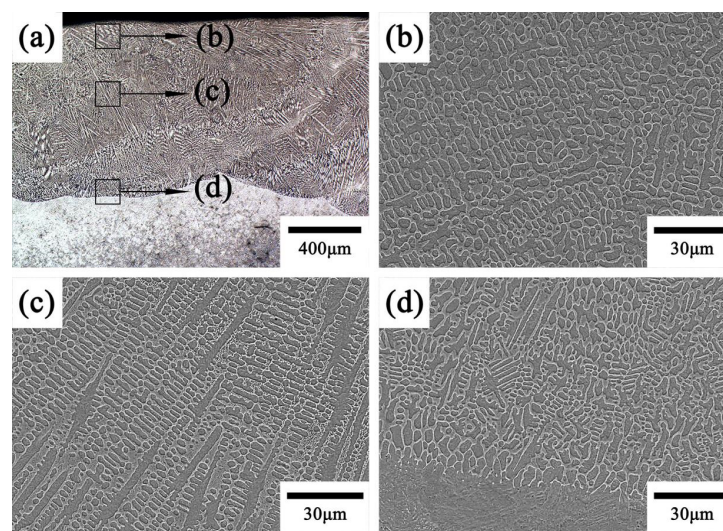


Figure 2. Typical structures of different regions of the laser cladding Co-based coating: (a) macrostructure of the cross-sectional morphology; (b) upper region; (c) middle region; (d) interface region.

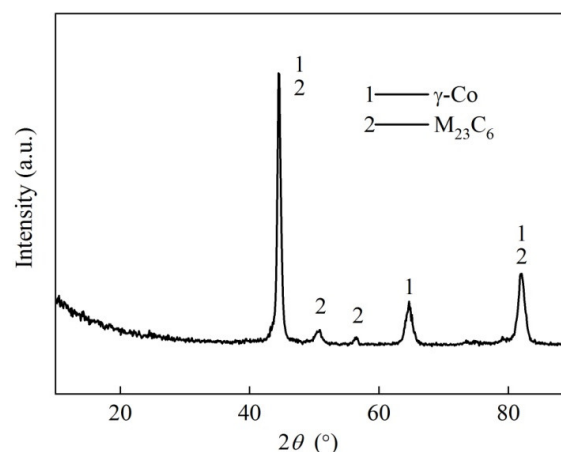


Figure 3. XRD patterns of the Co-based alloy cladding layer.

The EDX method was used to identify the elementary compositions of the different phases. As shown in Figure 4, the EDX results indicated that the dendrites were γ -Co and a γ -Co solid solution rich in Fe, Cr and Si, while the interdendritic phase was determined to be the $M_{23}C_6$ (M is Cr and Fe) eutectic phase with some WC and SiC. Owing to the large degree of undercooling, the Fe and Si exhibited as solid solution elements that stabilized

the γ -Co phase in the cooling process of the molten pool [19]. C could significantly improve the crystallization behavior during the solidification process, which further influenced the material properties. When a certain amount of the carbides was deposited at the grain boundary, a supportive skeleton network could be formed, which prevented the grain boundary from sliding and being eroded.

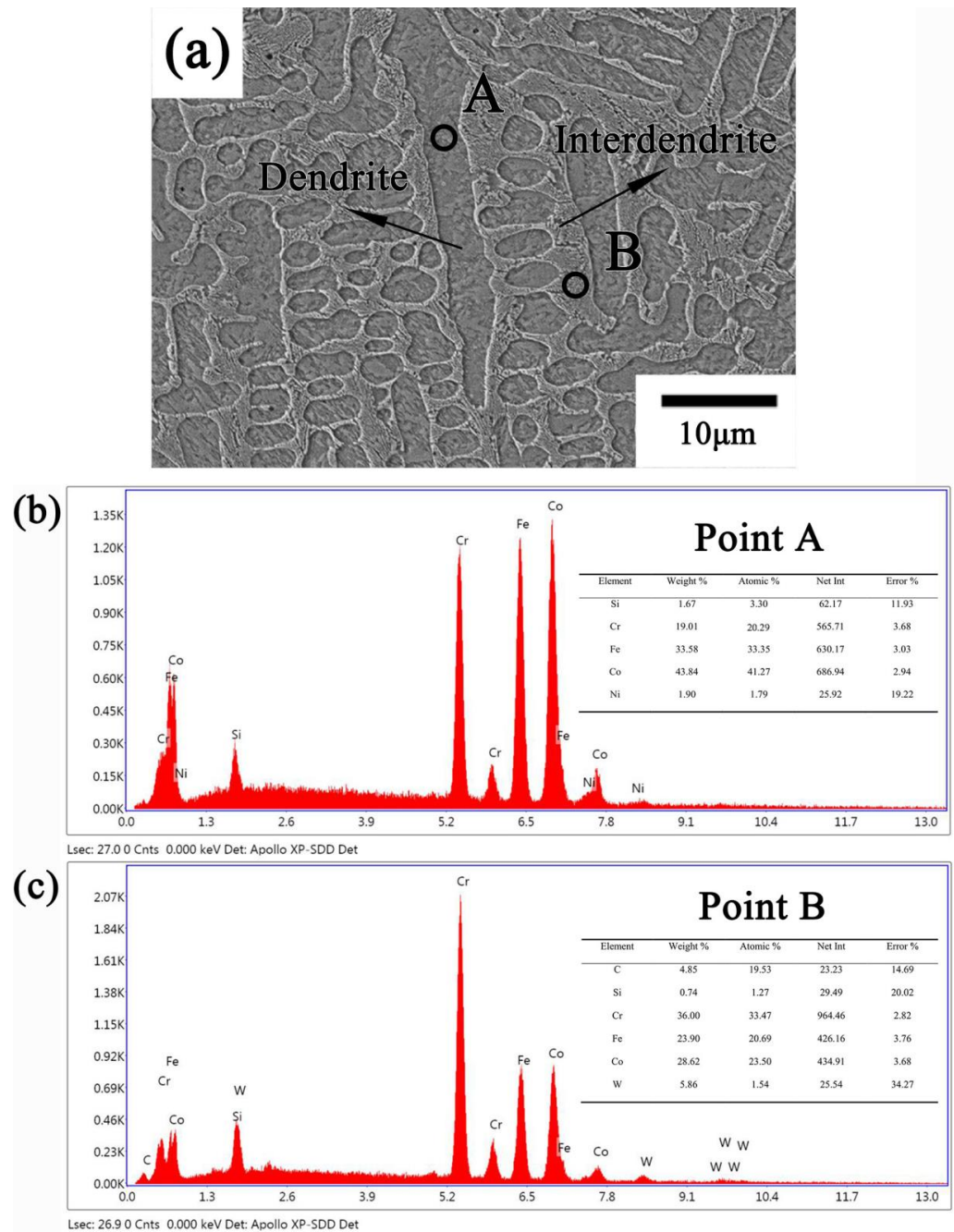


Figure 4. SEM-EDX analysis of the Co-based alloy cladding layer: (a) microstructural morphology at the top of the coating; (b) point scanning at point A; (c) point scanning at point B.

During the laser cladding process, the powder and the surface of the H13 steel substrate were melted under a high-energy input and then rapidly cooled, resulting in a diverse solidification microstructure in the molten pool. There are two important factors that significantly influence the ultimate solidification microstructure: the temperature gradient (G) and the solidification rate (R). Moreover, the value of the G/R ratio in the molten pool is a key factor in the final microstructural composition, according to the solidification

principle [21,22]. In the solidification process, the grain growth direction is opposite to the direction of thermal diffusion [23]. At the beginning of the cooling process, the molten pool firstly nucleates at the interface where the G between the molten pool and the matrix is extremely large and the R tends towards zero. The solidus–liquidus interface slowly advances in the molten pool along a positive temperature gradient. Following the initial stage, due to the R rapidly increasing and the G decreasing which results in a decrease in the G/R ratio, the grains tend to become cellular and transition to dendrite growth from planar growth. As the fastest heat loss is in the direction perpendicular to the interface, the solutes enriching the front end of the cellular grains during the solidification process lead to composition undercooling. Therefore, as shown in Figure 2c, the first and second layers of dendritic grains grew perpendicularly to the intersection and the dendrite arm, respectively. The reason for the appearance of equiaxed grains near the surface of the coating was the continuous increase in the solidification rate R and the variation in the heat dissipation direction in the molten pool under the influence of air convection.

As shown in Figure 5, the overlapping zone is mainly composed of coarse cellular and dendritic structures. In the laser cladding process, part of the well-solidified coating of the first layer was melted again when fabricating the second layer. As shown in previous research, the cooling rate between the overlapping zone and the molten pool decreases due to the absorption of heat from the high-energy laser beam [24]. Thus, the structure is different from the equiaxial structure shown in the first layer, with the cellular grains being coarse due to the length of incubation time in the overlapping zone.

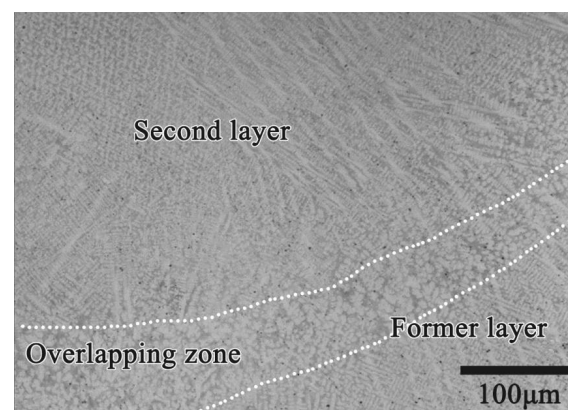


Figure 5. Microstructure at overlapping zone of the Co-based alloy cladding layer.

3.2. Hardness Distribution

The hardness distribution of the St6 Co-based laser cladding coating is shown in Figure 6. The hardness decreased from the surface of the coating to the substrate; at the same time, there was a transition region in the heat-affected zone. The average hardness value of the laser cladding coating was 732.6 HV_{0.5}, which was a 3.55-fold increase compared to the substrate hardness (206.2 HV_{0.5}). According to Estey et al. [25], the rapid cooling rate could produce grain refinement and solute retention, which improves the hardness of materials. During the hardness test, this would inhibit dislocation propagation, therefore exhibiting excellent hardness performance. Overall, the above hardness performance of the laser cladding coating is attributed to the dual effect of solution strengthening with Ni, Cr, and Si and dispersion strengthening with hard carbides. In addition, the hardness of the heat-affected zone was higher than that of the substrate as a consequence of the laser thermal radiation, which was equal to the quenching process, resulting in a dilution effect in which the heat affected zone was mainly composed of refined grains.

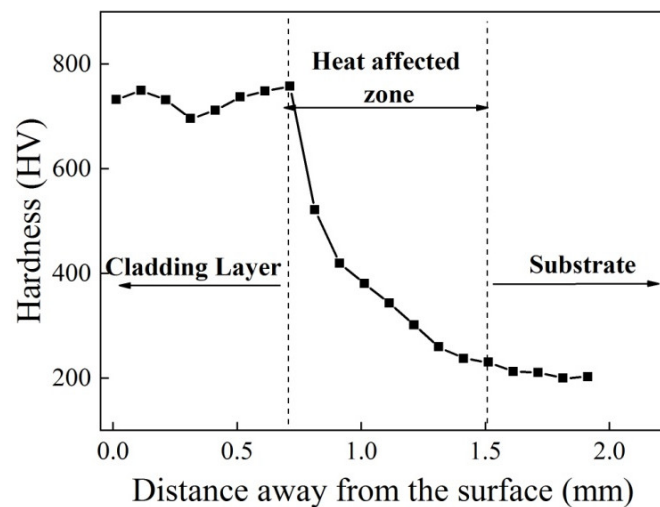


Figure 6. Hardness distribution of the Co-based alloy cladding layer.

3.3. Aluminum Corrosion Analysis

Figure 7 shows cross-sectional micrographs of the specimens under different corrosion durations in molten aluminum. The structure of the interface between the coating and molten Al was divided into three sub-interfaces (I, II and III) and four regions (coating, Layer A of IMCs, Layer B of IMCs, and Al). Interface I was very flat and the coating was tight without the tendency for dissociation. The Co-based alloy coating was partially dissolved after reacting with the molten aluminum, which exhibited as the intermetallic compounds (IMCs). As shown in Figure 7b, after 4 h of immersion, Interface III was sawtoothed, and there were fine needle-like, stripe-shaped and block-shaped compounds dissolved in the aluminum. For specimens after 8 h and 16 h of immersion, the IMCs in Layer B appeared massively broken, and there were also block- and needle-shaped compounds in the aluminum at Interface III. Although the IMCs in the thin and dense Layer A were scoured by aluminum liquid, the interface was not totally dissociated, which meant that IMCs in Layer A were tightly bonded with each other while the IMCs in Layer B were prone to be discrete. Moreover, there was an obvious peeling crack at Interface I, which was attributed to the different internal stresses between the coating and IMC layers resulting from the different thermal expansion coefficients during the aluminum liquid cooling process. After 24 h of immersion, the compounds appeared as small particles, most of which were dissolved in aluminum, shown in Figure 7g.

In addition, the elemental composition of the different zones for spots 1 to 11 in Figure 7 is shown in Table 3. It is observed that Al displayed a negative concentration gradient from the aluminum side to the Interface I. As the concentration of Al in Interface I increased from 55.2% to 61.7%, this suggests an increasing trend of Al concentration in Layer A with increasing immersion time. In particular, it should be noted that there was no Al at the spot 8, which indicates that the diffusion of Al stopped near Interface I and the Co-based alloy coating maintained its structural integrity.

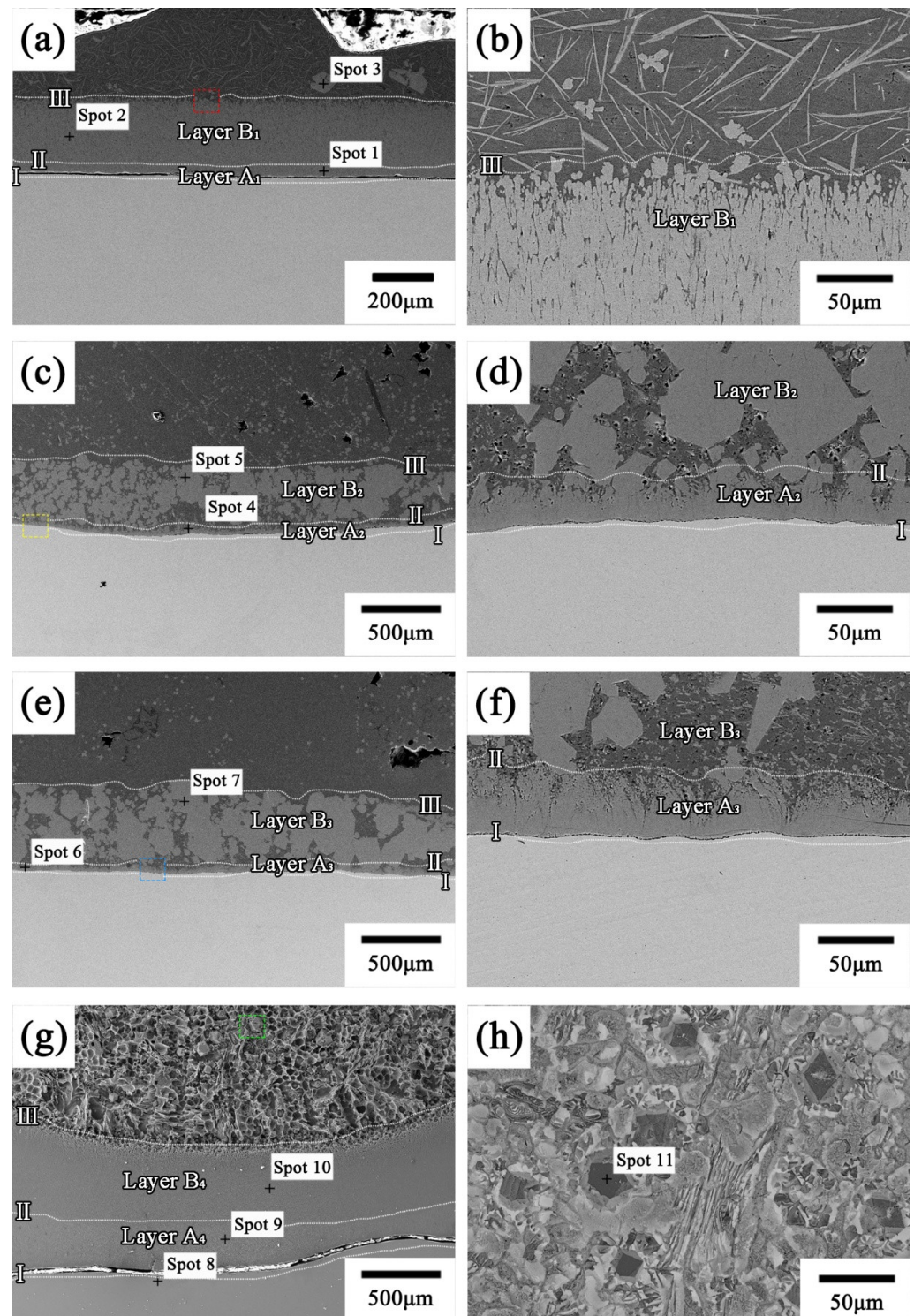


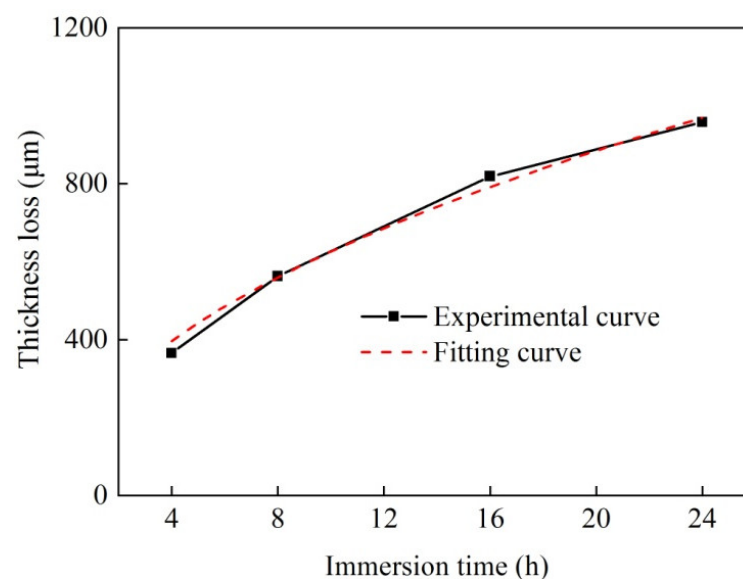
Figure 7. Cross-sectional SEM micrographs of the Co-based alloy cladding layer immersed in liquid aluminum for different times: (a) immersion for 4 h; (b) microstructure of the red square zone; (c) immersion for 8 h; (d) microstructure of the yellow square zone; (e) immersion for 16 h; (f) microstructure of the blue square zone; (g) immersion for 24 h; (h) microstructure of the green square zone.

Table 3. Elemental composition of different zones after aluminum corrosion (wt%).

Test point	Al	Co	Cr	Fe	Si	C
Spot1	55.2	0.3	7.4	17.7	8.9	0.7
Spot2	48.5	1.4	4.2	13.9	22.0	7.8
Spot3	55.3	-	4.3	22.0	8.2	7.1
Spot4	56.3	10.7	6.2	13.2	5.3	6.2
Spot5	57.2	2.6	7.9	16.0	7.2	5.1
Spot6	58.1	8.5	7.1	13.5	4.9	7.3
Spot7	56.1	2.9	7.5	15.5	6.6	7.1
Spot8	-	46.5	33.7	9.8	1.1	6.1
Spot9	61.7	16.1	11.1	5.6	3.9	1.6
Spot10	59.8	11.6	10.6	10.7	4.8	2.2
Spot11	62.8	-	7.4	16.6	9.9	3.4

3.4. Aluminum Corrosion Resistance Mechanism

In this study, the thickness of the IMCs was measured using Image J software to characterize the corrosion behavior of the Co-based alloy cladding layer. On the basis of classical kinetic theory [26], the thickness loss curve is approximately parabolic, as shown in the corrosion kinetics curve in Figure 8. This indicates that the thickness of the IMC layer was positively correlated with erosion time and the corrosion rate decreased with increases in erosion time.

**Figure 8.** The loss of thickness of the intermetallic compounds with immersion time.

The IMCs in different layers were examined using the XRD method to determine the aluminum corrosion behavior of the Co-based coating. As shown in Figure 9, the diffraction peaks were very close to the $(\text{Co, Fe, Cr})_2\text{Al}_9$, $(\text{Co, Fe, Cr})_2\text{Al}_5$ and $(\text{Fe, Cr})_4\text{Al}_{13}$ phases, respectively. Tang et al. [27] proved the existence of Co_2Al_9 using the EDX and TEM approaches when studying the interface reaction between a Co–Cr–Mo alloy and liquid Al. Besides the presence of the above-mentioned phases, the diffraction peaks of M_{23}C_6 precipitations were also found in the XRD results. According to the above EDS results and the peak positions, this suggests an identification as the Cr_{23}C_6 precipitation. Therefore, while the γ -Co phase at the Interface III was completely dissolved, the Cr_{23}C_6 in the coating did not completely react with the molten aluminum after 24 h immersion. At the same time, it could be found that Layer A of the IMCs obtained more Co and Layer B of the IMCs obtained more Al, Cr, Fe and Si, as shown in Table 3. Similar to point 3, the compound at point 11 exhibited a high Al content without Co. This indicates that the

granular compound in the aluminum solution was gradually decomposed as immersion time increased, until completely dissolved. Thus, combined with the Al–Si, Al–Co and Al–C phase diagrams [28–30], it is speculated that Layer B of the IMCs was composed of the $(\text{Co, Fe, Cr})_2\text{Al}_9$ and $(\text{Fe, Cr})_4\text{Al}_{13}$ phases, while Layer A of the IMCs was composed the $(\text{Co, Fe, Cr})_2\text{Al}_5$ phase. At 1013 K, the solubility of Co and Cr in liquid Al are 1.53 at% and 0.58 at%, respectively, which assumes that the formation of the $(\text{Fe, Cr})_4\text{Al}_{13}$ phase in Layer B of the IMCs is caused by the high solubility of Co in liquid Al [31,32]. In the solidus–liquidus Al reaction system, the Co_2Al_5 layer firstly forms at the solidus–liquidus interface in a short period of time before reaching the equilibrium of formation and dissolution [33]. Similarly, the formation and dissolution of the $(\text{Co, Fe, Cr})_2\text{Al}_9$ layer could rapidly reach an equilibrium state and the corrosion of Co-based alloy cladding was mainly controlled by the dissolution of the $(\text{Co, Fe, Cr})_2\text{Al}_9$ in Layer B of the IMCs.

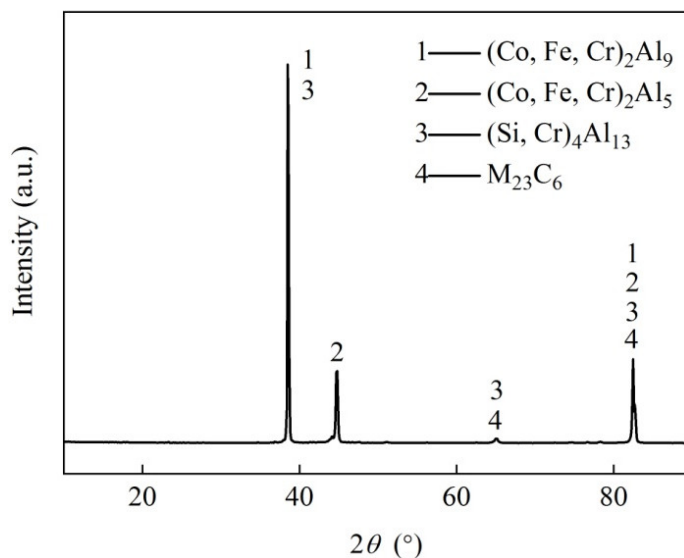
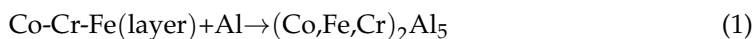


Figure 9. XRD patterns of the intermetallic compounds generated by the Co-based alloy cladding layer immersed in liquid aluminum for 24 h.

A schematic illustration of resistance to molten aluminum corrosion enhanced by the laser cladding Co-based alloy coating of the H13 steel surface is shown in Figure 10. Overall, the reactions in static aluminum liquid corrosion occurred in the sub-interfaces; the specific reaction mechanism could be explained as follows. At Interface I, Al atoms which diffused from the liquid Al reacted with the coating and formed the $(\text{Co, Fe, Cr})_2\text{Al}_5$ phase in the following reaction:



In Layer A of the IMCs, Al, Co, Cr, and Fe were interdiffused in the intermetallic compound layer. At Interface II, the $(\text{Co, Fe, Cr})_2\text{Al}_5$ phase continued to react with Al atoms which diffused from liquid Al, and formed the $(\text{Co, Fe, Cr})_2\text{Al}_9$ phase in the following reaction:



Similar to Layer A of the IMCs, the Al, Co, Cr, and Fe in Layer B of the IMCs were also interdiffused into each other. Owing to the high solubility of Co in liquid Al, it easily dissolved into liquid Al as the $(\text{Co, Fe, Cr})_2\text{Al}_9$ phase further formed along with the $(\text{Fe, Cr})_4\text{Al}_{13}$ phase.



At Interface III, Layer B of the IMCs dissolved into the liquid Al and then diffused away in the following reaction:

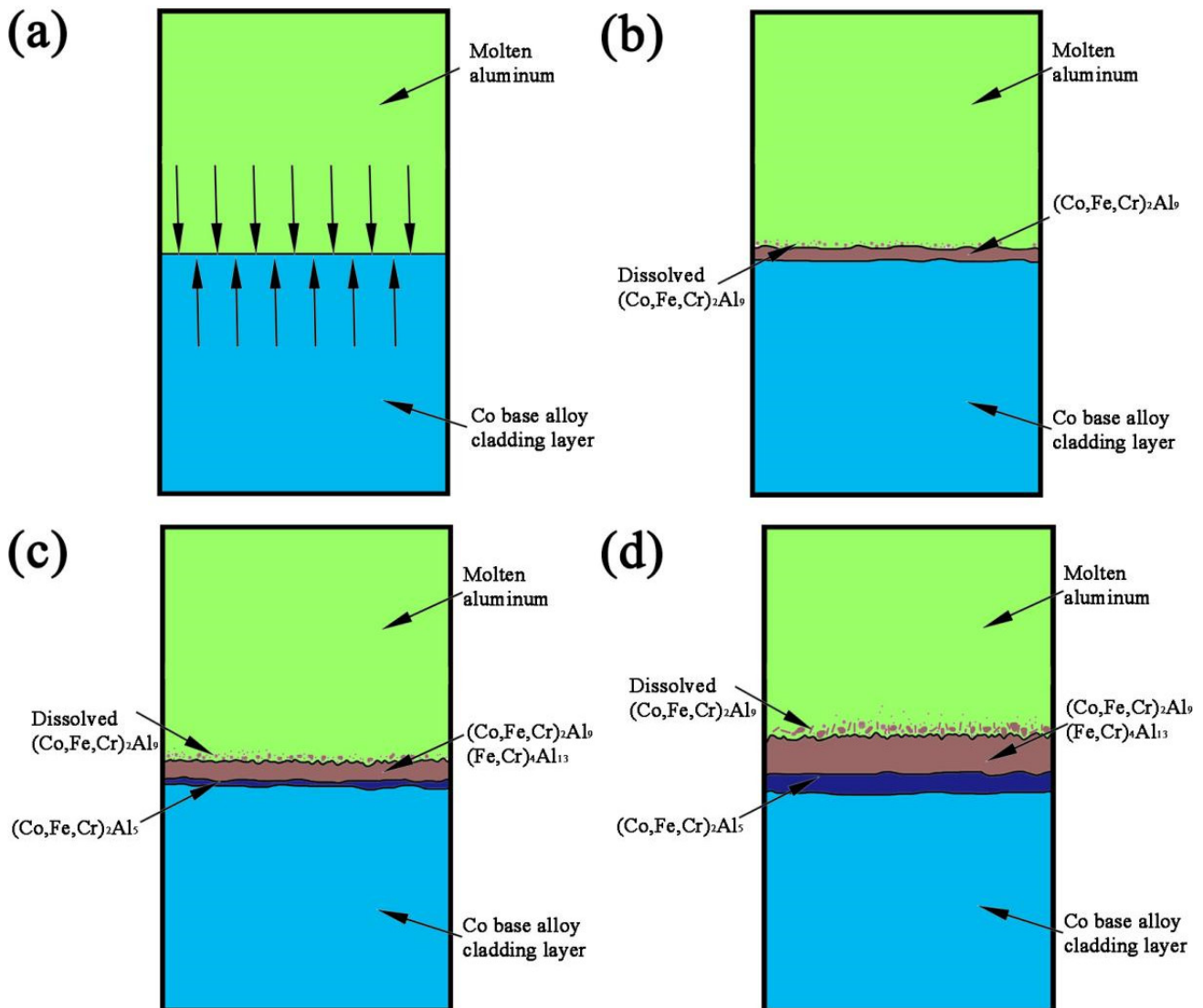
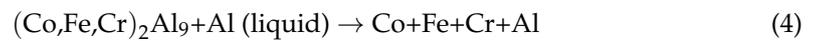


Figure 10. Schematic illustration of resistance to molten aluminum corrosion as enhanced by laser cladding Co-based alloy coating on H13 steel surface: (a) the initial stage of the aluminum erosion; (b) the formation of the IMCs in Layer A; (c) the formation of the IMCs in Layer B and (d) the stable stage of the aluminum erosion.

At the beginning of the immersion test, the Co-based alloy clad layer was firstly wetted by the aluminum liquid, after which the elements inter-diffused at the solidus–liquidus interface. The Co, Fe, Cr and Si in the cladding layer diffused into the molten aluminum which reacted to form the $(\text{Co, Fe, Cr})_2\text{Al}_9$ compound until the dissolution was saturated. As shown in Figure 10b, the formation and dissolution of the $(\text{Co, Fe, Cr})_2\text{Al}_9$ layer could reach an equilibrium state in a short time. Due to the high solubility of the Co element in liquid Al, the $(\text{Fe, Cr})_4\text{Al}_{13}$ compound could be formed between the $(\text{Co, Fe, Cr})_2\text{Al}_9$ layer and the liquid Al. With the elements continuing to inter-diffuse, a $(\text{Co, Fe, Cr})_2\text{Al}_5$ layer between the $(\text{Co, Fe, Cr})_2\text{Al}_9$ layer and the coating could be formed, as shown in

Figure 10c. The thickness of the IMCs gradually increased with immersion time. Interface I would move towards the coating side due to consumption of the Co-based alloy cladding, and with this being accompanied by Interface II moving towards the coating side, the compounds at Interface II were continuously dissolved in liquid Al. It is assumed that the loss of thickness the Co-based alloy cladding was due to the movement of Interface I, while the thickness evolution of the IMCs was the result of the relative movement of Interface I and Interface II. Finally, due to the internal stresses between various phases caused by the different thermal expansion coefficients, the compounds at Interface II were flaked into the liquid aluminum in small pieces during the cooling process.

4. Conclusions

In this study, a crack-free, homogeneous and dense St6-Co alloy coating with good metallurgical bonding to an H13 steel substrate was successfully prepared via a laser cladding process with optimized parameters. Planar grains were observed in the interface followed by cellular grains, columnar dendrites, dendrite structures and equiaxed dendrites in order from the substrate to the surface of the coating. The Co-based alloy coating was mainly composed of the γ -Co phase and $M_{23}C_6$ precipitation. The supersaturated metastable solid solution of Co, Fe and Si in γ -Co phase played a significant role in stabilizing the γ -Co matrix. The hardness decreased from the surface of the coating to the substrate due to the solution strengthening of Ni, Cr, and Si and dispersion strengthening of carbide precipitations, yielding a coating hardness 3.55 times that of the H13 substrate.

The corrosion kinetic curve shows that the thickness of the IMCs increased exponentially, which indicates that the corrosion rate gradually decreased with increasing immersion time. The $Cr_{23}C_6$ precipitation, which was not completely dissociated in the molten aluminum, showed great effect in hindering the diffusion of Fe and Al atoms. The St6-Co alloy coating was uniformly corroded by the liquid Al as two intermediate layers between the coating and the liquid Al with a $(Co, Fe, Cr)_2Al_9$ layer nearer to the coating side and $(Fe, Cr)_4Al_{13}$ and $(Co, Fe, Cr)_2Al_5$ layers nearer to the solidifying Al side. After 24 h of static corrosion in molten aluminum at 700 °C, the Co-based alloy coating could still maintain its integrity to protect the substrate.

Author Contributions: R.L. data curation, investigation, writing—original draft, M.Z.; conceptualization, writing—review and editing, methodology. J.Y.; writing—review and editing, data curation, Q.Y.; resources, writing—review and editing, S.G.; conceptualization, writing—review and editing, methodology. All authors have read and agreed to the published version of the manuscript.

Funding: This research was funded by Natural Science Foundation of Hebei Province (Grant No. 4540747).

Institutional Review Board Statement: Not applicable.

Informed Consent Statement: Not applicable.

Data Availability Statement: Not applicable.

Conflicts of Interest: The authors declare no conflict of interest.

References

1. Arif, A.F.M.; Sheikh, A.K.; Qamar, S.Z. A study of die failure mechanisms in aluminum extrusion. *J. Mater. Process. Technol.* **2003**, *134*, 318–328. [[CrossRef](#)]
2. Cheng, W.; Wang, C. Effect of chromium on the formation of intermetallic phases in hot-dipped aluminide Cr–Mo steels. *Appl. Surf. Sci.* **2013**, *277*, 139–145. [[CrossRef](#)]
3. Chen, G.; Wang, J.; Wang, D.; Xue, L.; Zeng, B.; Qin, B.; Tang, Z. Effect of liquid oxy-nitriding at various temperatures on wear and molten aluminum corrosion behaviors on AISI H13 steel. *Corros. Sci.* **2020**, *178*, 109088. [[CrossRef](#)]
4. Terčelj, M.; Smolej, M.A.; Fajfar, P.; Turk, R. Laboratory assessment of wear on nitrided surfaces of dies for hot extrusion of aluminium. *Tribol. Int.* **2007**, *40*, 374–384. [[CrossRef](#)]
5. Wang, Q.; Wang, W.; Liu, H.; Zeng, C. Corrosion behavior of zirconium diboride coated stainless steel in molten 6061 aluminum alloy. *Surf. Coat. Technol.* **2017**, *313*, 129–135. [[CrossRef](#)]

6. Zhang, X.; Li, X.; Chen, W. Interfacial reactions of duplex stainless steels with molten aluminum. *Surf. Interface Anal.* **2015**, *47*, 648–656. [[CrossRef](#)]
7. Zhang, X.; Chen, W. Review on corrosion-wear resistance performance of materials in molten aluminum and its alloys. *Trans. Nonferrous Met. Soc. China* **2015**, *25*, 1715–1731. [[CrossRef](#)]
8. Weng, F.; Chen, C.; Yu, H. Research status of laser cladding on titanium and its alloys: A review. *Mater. Des.* **2014**, *58*, 412–425. [[CrossRef](#)]
9. Sexton, L.; Lavin, S.; Byrne, G.; Kennedy, A. Laser cladding of aerospace materials. *J. Mater. Process. Technol.* **2002**, *122*, 63–68. [[CrossRef](#)]
10. Liu, J.; Yu, H.; Chen, C.; Weng, F.; Dai, J. Research and development status of laser cladding on magnesium alloys: A review. *Opt. Lasers Eng.* **2017**, *93*, 195–210. [[CrossRef](#)]
11. Lu, P.; Lewis, S.R.; Fretwell-Smith, S.; Engelberg, D.L.; Fletcher, D.I.; Lewis, R. Laser cladding of rail; the effects of depositing material on lower rail grades. *Wear* **2019**, *438–439*, 203045. [[CrossRef](#)]
12. Joshi, V.; Srivastava, A.; Shivpuri, R. Intermetallic formation and its relation to interface mass loss and tribology in die casting dies. *Wear* **2004**, *256*, 1232–1235. [[CrossRef](#)]
13. Khan, F.F.; Bae, G.; Kang, K.; Kumar, S.; Jeong, T.; Lee, C. Development of cermet coatings by kinetic spray technology for the application of die-soldering and erosion resistance. *Surf. Coat. Technol.* **2009**, *204*, 345–352. [[CrossRef](#)]
14. Chen, G.; Wang, J.; Fan, H.; Wang, D.; Li, X.; Dong, H. Combat molten aluminum corrosion of AISI H13 steel by low-temperature liquid nitrocarburizing. *J. Alloy. Compd.* **2019**, *776*, 702–711. [[CrossRef](#)]
15. López, A.J.; Rams, J. Protection of carbon steel against molten aluminum attack and high temperature corrosion using high velocity oxygen-fuel WC–Co coatings. *Surf. Coat. Technol.* **2015**, *262*, 123–133. [[CrossRef](#)]
16. Vasić, M.M.; Žák, T.; Pizúrová, N.; Roupčová, P.; Minić, D.M. Thermally induced microstructural transformations and anti-corrosion properties of Co₇₀Fe₅Si₁₀B₁₅ amorphous alloy. *J. Non. Cryst. Solids.* **2018**, *500*, 326–335. [[CrossRef](#)]
17. CZenk, C.H.; Bauer, A.; Goik, P.; Neumeier, S.; Stone, H.J.; Göken, M. Microstructure, Lattice misfit, and high-temperature strength of γ' -strengthened Co–Al–W–Ge model superalloys. *Metall. Mater. Trans. A Phys. Metall. Mater. Sci.* **2016**, *47*, 2141–2149.
18. Zhao, J.; Gao, Q.; Wang, H.; Shu, F.; Zhao, H.; He, W.; Yu, Z. Microstructure and mechanical properties of Co-based alloy coatings fabricated by laser cladding and plasma arc spray welding. *J. Alloy. Compd.* **2019**, *785*, 846–854. [[CrossRef](#)]
19. Yan, H.; Wang, A.; Xu, K.; Wang, W.; Huang, Z. Microstructure and interfacial evaluation of Co-based alloy coating on copper by pulsed Nd:YAG multilayer laser cladding. *J. Alloy. Compd.* **2010**, *505*, 645–653. [[CrossRef](#)]
20. Shu, F.; Wu, L.; Zhao, H.; Sui, S.; Zhou, L.; Zhang, J.; He, W.; He, P.; Xu, B. Microstructure and high-temperature wear mechanism of laser clad CoCrBFeNiSi high-entropy alloy amorphous coating. *Mater. Lett.* **2018**, *211*, 235–238. [[CrossRef](#)]
21. Wang, G.; Zhang, J.; Shu, R.; Yang, S. High temperature wear resistance and thermal fatigue behavior of Stellite-6/WC coatings produced by laser cladding with Co-coated WC powder. *Int. J. Refract. Met. Hard Mater.* **2019**, *81*, 63–70. [[CrossRef](#)]
22. Hidouci, A.; Pelletier, J.M.; Ducoin, F.; Dezert, D.; El Guerjouma, R. Microstructural and mechanical characteristics of laser coatings. *Surf. Coat. Technol.* **2000**, *123*, 17–23. [[CrossRef](#)]
23. Lu, H.; Li, W.; Qin, E.; Liu, C.; Liu, S.; Zhang, W.; Wu, S. The gradient microstructure and high-temperature wear behavior of the cocrmosi coating by laser cladding. *J. Therm. Spray Technol.* **2020**, *30*, 968–976. [[CrossRef](#)]
24. Cui, C.; Guo, Z.; Liu, Y.; Xie, Q.; Wang, Z.; Hu, J.; Yao, Y. Characteristics of cobalt-based alloy coating on tool steel prepared by powder feeding laser cladding. *Opt. Laser Technol.* **2007**, *39*, 1544–1550. [[CrossRef](#)]
25. Estey, C.M.; Cockcroft, S.L.; Maijer, D.M.; Hermesmann, C. Constitutive behaviour of A356 during the quenching operation. *Mater. Sci. Eng. A.* **2004**, *383*, 245–251. [[CrossRef](#)]
26. Pouraliakbar, H.; Khalaj, G.; Lidija Gomidželović, L.; Khalaj, M.J.; Nazerfakhari, M. Duplex ceramic coating produced by low temperature thermo-reactive deposition and diffusion on the cold work tool steel substrate: Thermodynamics, kinetics and modeling. *Ceram. Int.* **2015**, *41*, 9350–9360. [[CrossRef](#)]
27. Tang, N.; Li, Y.; Koizumi, Y.; Kurosu, S.; Chiba, A. Interfacial reaction between Co–Cr–Mo alloy and liquid Al. *Corros. Sci.* **2013**, *75*, 262–268. [[CrossRef](#)]
28. Wang, Y.; Vecchio, K.S. Microstructure evolution in Fe-based-aluminide metallic-intermetallic laminate (MIL) composites. *Mater. Sci. Eng. A* **2016**, *649*, 325–337. [[CrossRef](#)]
29. Shi, Z.; Cao, J.; Han, F. Preparation and characterization of Fe–Al intermetallic layer on the surface of T91 heat-resistant steel. *J. Nucl. Mater.* **2014**, *447*, 77–81. [[CrossRef](#)]
30. Takata, N.; Nishimoto, M.; Kobayashi, S.; Takeyama, M. Crystallography of Fe₂Al₅ phase at the interface between solid Fe and liquid Al. *Intermetallics* **2015**, *67*, 1–11. [[CrossRef](#)]
31. Gödecke, T.; Ellner, M. Phase equilibria in the Al-rich portion of the ternary system Co–Ni–Al at 75 and 78 at.% Al. *Zeitschrift Fuer Met. Res. Adv. Tech.* **1997**, *88*, 382–389.
32. Murray, J.L. The Al–Cr (aluminum-chromium) system. *J. Phase Equilibria Diffus.* **1998**, *19*, 367–375. [[CrossRef](#)]
33. Tang, N.; Li, Y.; Koizumi, Y.; Kurosu, S.; Chiba, A. Experimental and theoretical research on interfacial reaction of solid Co with liquid Al. *Corros. Sci.* **2003**, *73*, 54–61. [[CrossRef](#)]